

A comprehensive separation of dark matter and baryonic mass components in galaxy clusters I: Mass constraints from Abell S1063

Benjamin Beauchesne,^{1,2*} Benjamin Clément,³ Marceau Limousin,⁴ Belén Alcalde Pampliega,^{5,6,7} Mathilde Jauzac,^{1,2,8,9} Anna Niemiec,¹⁰ Johan Richard,¹¹ Guillaume Mahler,¹² Jose M. Diego,¹³ Pascale Hibon,⁵ Anton M. Koekemoer,¹⁴ Thomas Connor,¹⁵ Jean-Paul Kneib,³ Andreas L. Faist¹⁶

¹Centre for Extragalactic Astronomy, Department of Physics, Durham University, South Road, Durham DH1 3LE, UK

²Institute for Computational Cosmology, Department of Physics, Durham University, South Road, Durham DH1 3LE, UK

³Institute of Physics, Laboratory of Astrophysics, Ecole Polytechnique Fédérale de Lausanne (EPFL), Observatoire de Sauverny, 1290 Versoix, Switzerland

⁴Aix Marseille Univ, CNRS, CNES, LAM, Marseille, France

⁵ESO Vitacura, Alonso de Córdova 3107, Vitacura, Casilla 19001, Santiago de Chile, Chile

⁶Instituto de Estudios Astrofísicos, Facultad de Ingeniería y 455 Ciencias, Universidad Diego Portales, Av. Ejército Libertador 441, Santiago, Chile

⁷SKA Observatory, Jodrell Bank, SK11 9FT, UK

⁸Astrophysics Research Centre, University of KwaZulu-Natal, Westville Campus, Durban 4041, South Africa

⁹School of Mathematics, Statistics & Computer Science, University of KwaZulu-Natal, Westville Campus, Durban 4041, South Africa

¹⁰Univ. Grenoble Alpes, CNRS, Grenoble INP, LPSC IN2P3, 53, Avenue des Martyrs, 38000 Grenoble, France

¹¹Univ Lyon, Univ Lyon1, Ens de Lyon, CNRS, Centre de Recherche Astrophysique de Lyon (CRAL) UMR5574, F-69230 Saint-Genis-Laval, France

¹²STAR Institute, Quartier Agora - Allée du six Août, 19c B-4000 Liège, Belgium

¹³Instituto de Física de Cantabria (CSIC-UC). Avda. Los Castros s/n. 39005 Santander, Spain

¹⁴Space Telescope Science Institute, 3700 San Martin Dr., Baltimore, MD 21218, USA

¹⁵Center for Astrophysics | Harvard & Smithsonian, 60 Garden St., Cambridge, MA 02138, USA

¹⁶Caltech/IPAC, 1200 E. California Blvd. Pasadena, CA 91125, USA

Accepted XXX. Received YYY; in original form ZZZ

ABSTRACT

In this two-part series, we present a multi-probe mass modelling method for massive galaxy clusters, designed to disentangle the contributions of individual mass components (Dark matter, intra-cluster gas, stellar masses). In this first paper, we focus on recovering the mass constraint datasets required for the modelling approach introduced in the second paper. Specifically, we measure the light distribution, stellar mass, and kinematics of the cluster members, the brightest cluster galaxy (BCG), and the intra-cluster light (ICL) in Abell S1063. To that end, we developed a new method to extract the light profiles of the cluster members, BCG, and ICL, while accounting for contamination from nearby foreground and background galaxies in HUBBLE SPACE TELESCOPE (HST) imaging. We obtained light profiles for 289 cluster members using a dual Pseudo-Isothermal Elliptical (dPIE) model based on the HST F160W filter, while the BCG & ICL is modelled as a single component using a multi-Gaussian expansion. To estimate stellar masses and velocity dispersions, we rely on multi-band HST photometry and VLT/MUSE integral field spectroscopy, respectively. Stellar masses are derived using three different spectral energy distribution (SED) models. We measure the line-of-sight velocity dispersions of the cluster members at their half-light radii, as determined from their light profiles, while for the BCG & ICL components, we use elliptical annular apertures. Thanks to these measurements, we will be able to constrain the cluster stellar mass content, which is detailed in the second paper of the series. We publicly release these measurements with intermediary data products.

Key words: galaxies: clusters: general – galaxies: clusters: individual: Abell S1063 – Galaxy: kinematics and dynamics – Galaxy: stellar content

1 INTRODUCTION

In the context of the standard Λ cold dark matter (Λ CDM) cosmological model, galaxy clusters are the largest gravitationally bound structures and they are largely dominated by dark matter (DM). In

* E-mail: benjamin.e.beauchesne@durham.ac.uk

that regard, they are among the best natural laboratories to study DM properties (Clowe et al. 2004; Bradač et al. 2008; Natarajan et al. 2017) and its (possible) deviation from the CDM paradigm (Harvey et al. 2015; Meneghetti et al. 2020; Limousin et al. 2022; Andrade et al. 2022; Eckert et al. 2022). Statistical analyses of their properties allow us to put constraints on DM parameters such as an upper bound on the DM interaction cross-section (Sagunski et al. 2021; Andrade et al. 2022; Eckert et al. 2022). The study of outliers in the cluster population, such as the bullet cluster, has brought evidence in favour of the DM paradigm (Clowe et al. 2006) while challenging modified theories of gravity (Brownstein & Moffat 2007; Dai et al. 2008).

As DM manifests itself through gravitational interactions, its observational studies in clusters rely on mass modelling methods. Different probes can be used, such as the heating of the intra-cluster gas, allowing for a total mass estimation if the cluster follows the hydrostatic equilibrium (Ettori et al. 2013), or the dynamics of the cluster members, which are floating in the overall cluster gravitational potential well (Mamon et al. 2013; Mamon 2022). Among these probes, gravitational lensing is a frontrunner, as it only relies on projection hypotheses instead of cluster relaxation states or symmetry. This phenomenon refers to the bending of light near a massive object, in our case, a galaxy cluster, which permits us to probe the projected gravitational potential. At the core of the cluster, we are in the strong gravitational lensing regime where the background object appears highly distorted to observers, forming giant arcs and/or appearing multiple times in the cluster field. This last phenomenon is referred to as the multiple image phenomenon, which forms the main constraints used by strong lensing modelling methods (see Kneib & Natarajan (2011); Natarajan et al. (2024) for reviews on this topic).

Each of these mass probes can help derive relevant constraints on DM properties by mapping the total mass distribution. Hydrostatic analyses of galaxy clusters thanks to X-ray observations combined with large-scale simulation measurements have set an upper bound on the DM cross-section (Eckert et al. 2022) of self-interacting dark matter (Spergel & Steinhardt 2000, SIDM). Andrade et al. (2022) obtained similar constraints by fitting the lensing profile with a phenomenological SIDM model (Robertson et al. 2021). However, none of these methods accurately measure the DM profile as baryons in cluster members or intra-cluster gas are usually not modelled and accounted for in the total mass budget. This baryonic fraction can reach up to 20 per cent of the total mass, primarily due to the contribution of the gas (Bonamigo et al. 2018; Beauchesne et al. 2024). Considering such baryonic contributions is important to compare observational results with large-scale simulations as the measurements can agree on the total mass profile while presenting discrepancies with respect to the DM distributions.

To obtain an accurate census on DM, each cluster baryonic component has to be accounted for and thus constrained. Several analyses provided methods to account for the intra-cluster gas in the context of lensing analyses via different optimisation approaches (Sereno et al. 2010; Bonamigo et al. 2017, 2018; Beauchesne et al. 2024). In particular, Beauchesne et al. (2024, B24 hereafter) provided a self-consistent framework to combine lensing and X-ray observations in a single process, where the mass model is constrained by a likelihood combining these two sets of constraints. Such a framework can be extended to include other types of constraints, such as the stellar kinematics of the brightest cluster galaxy (BCG). This galaxy sits at the centre of the cluster mass distribution, which lacks lensing features, but can offer valuable constraints on the SIDM cross-section (Sagunski et al. 2021). Newman et al. (2013) and Cerny et al. (2025) provided a decomposition of DM and baryons in the BCG based on lensing and stellar kinematic constraints, allowing them to report a

deviation from the CDM paradigm with a flatter inner DM slope. Combining such an approach with the method used in B24 would allow us to constrain the innermost part of the cluster where the BCG sits, while providing an exhaustive mapping of baryons via the inclusion of the intra-cluster gas. Additionally, intra-cluster stars, from which the intra-cluster light (ICL; see Montes 2022, for a review) originates, can be used to extend such constraints. Similarly to the BCG stellar kinematics, probing the BCG total mass distribution, the same measurement from ICL stars can constrain the cluster total mass profile. Both components are known to present different patterns as the velocity dispersion of the stellar distribution is known to increase from the BCG to the ICL (Longobardi et al. 2018). Adding a mass component representing the ICL in a mass model similar to B24, would allow us to disentangle all main mass components at the cluster scale: DM, intra-cluster gas and intra-cluster stars.

In this series of papers, we aim to present a modelling method that accounts for each main mass component of the cluster to fully separate DM from baryonic masses. As state-of-the-art cosmological simulations are now hydrodynamic and thus include baryonic physics, cluster mass models have to be more detailed to properly compare observed DM distributions as well as the interplay with baryons. The main focus of this series is to combine the B24 approach, which includes the intra-cluster gas with Newman et al. (2013) method extended to account for the ICL, allowing for resulting mass models to include all cluster main mass components. As DM will be disentangled at the cluster scale, we will also detail a new modelling of cluster members, based on a baryonic/DM decomposition, to fully disentangle DM from baryons down to the galaxy scale. We organise this series in two papers, in the first and current one, we present the mass constraints and, in particular, how we recover the supplementary constraints required to map the stellar mass distribution. In the second paper (Hereafter B25b Beauchesne 2025), we focus on the modelling method and the reliability of the stellar mass estimate.

We test this new method on a well-studied and observationally constrained cluster, Abell S1063 (Abell et al. 1989). The mass distribution of Abell S1063 has been studied multiple times using strong gravitational lensing (Monna et al. 2014; Johnson et al. 2014; Richard et al. 2014; Zitrin et al. 2015; Caminha et al. 2016; Diego et al. 2016; Bonamigo et al. 2018; Bergamini et al. 2019; Granata et al. 2022; Limousin et al. 2022; Andrade et al. 2022, B24). Due to its morphology simplicity and wealth of observational data as one of the Hubble Frontier Field clusters (Lotz et al. 2017), this cluster has been used as a test case for modelling improvement with the work of Bonamigo et al. (2018); Bergamini et al. (2019); Granata et al. (2022) and B24. It is also the main motivation behind the present work, in addition to reusing the same modelling of the gas mass as in B24.

In this first paper, we present the test object along with the observational datasets in Sect. 2. In Sect. 3, we present the pre-existing mass constraints, i.e. strong lensing and X-ray observations. In Sect. 4, we detail how we extract cluster member constraints using their light distribution (Sect. 4.1), stellar kinematics (Sect. 4.2) and stellar masses (Sect. 4.3). We then describe the measurements of the same quantities for the BCG and the ICL from Sect. 5 to Sect. 5.1, 5.2 and 5.3.

Throughout this work, we adopt a flat Λ CDM cosmology with $\Omega_\Lambda = 0.7$, $\Omega_m = 0.3$ and $H_0 = 70 \text{ km s}^{-1} \text{ Mpc}^{-1}$. Magnitudes are quoted in the AB system. Regarding the statistical treatment of all the analyses, we compute uncertainties with the median-centred credible intervals (CI) based on the posterior distribution of the considered random variable. We refer to the interval containing $100 \times \text{erf}\left(\frac{n}{\sqrt{2}}\right)$

per cent of the posterior with n an integer by $n\sigma$ CI. If we use σ to denote a standard deviation, we explicitly notify it in the text.

2 TEST OBJECT: ABELL S1063

Galaxy cluster Abell S1063 (AS1063; also known as RXC J2248.7-4431 and SPT-CL J2248-4431), is a massive galaxy cluster at $z = 0.3475$, first identified by [Abell et al. \(1989\)](#). It is an ideal laboratory for this work as it has a fairly simple morphology for the amount of archival observations available. We refer the reader to the argument presented in B24 about this choice, as they are similar and the methodology presented in this work is an extension of the B24 one. To set-up the general observational context, we show in Fig. 1 a composite colour image of the cluster made with the *Hubble Space Telescope* (HST) broad band filters: F435W (blue), F606W (green) and F814W (red). We present in Fig. 1 the X-ray surface brightness and the footprint of the spectroscopic observations from the Very Large Telescope (VLT)/Multi Unit Spectroscopic Explorer (MUSE) ([Bacon et al. 2010](#)). We introduce each observational dataset in the following sections (X-rays in Sect. 2.1, and optical imaging and spectroscopy in Sect. 2.2 and 2.3).

2.1 X-ray observations

We use archival observations from the *Chandra X-ray observatory* of AS1063 as our X-ray datasets. These observations are contained in the *Chandra* Data Collection (CDC) 389 [doi:10.25574/cdc.389](https://doi.org/10.25574/cdc.389). Their combined observing times account for 123 ks. Regarding the reduction and analysis of those datasets, we use the same reduction and analysis as B24, and we refer the reader to that reference for the detailed procedure.

2.2 Photometric data

AS1063 has been extensively observed with the HUBBLE SPACE TELESCOPE (HST) through multiple programs, including The Cluster Lensing And Supernova survey with Hubble (CLASH; [Postman et al. 2012](#)); the Hubble Frontier Fields (HFF; [Lotz et al. 2017](#)), and the Beyond Ultra-deep Frontier Fields And Legacy Observations (BUFFALO; [Steinhardt et al. 2020](#)). The bulk of the observations is formed by the HFF dataset that has been spatially extended with the BUFFALO program.

For the following analyses, we use the mosaic images reprocessed by the BUFFALO collaboration, combining all available HST observations in the filters obtained by the HFF program. All the HST exposures from these programs had been recalibrated using the latest reference files, aligned to Gaia-DR3¹, and combined into mosaics at a pixel scale of $0''.03$, following the techniques first described by [Koekemoer et al. \(2011\)](#), updated for these new programs. For the complete description of the datasets, we refer the reader to [Lotz et al. \(2017\)](#) and [Steinhardt et al. \(2020\)](#) for the HFF and BUFFALO programs, respectively. The BUFFALO collaboration has produced weak lensing catalogues, although we are not making use of them in this work. They will be presented in the forthcoming work of Niemiec et al. (in prep).

2.3 Spectroscopic data

AS1063 was observed by MUSE with two pointings covering the South-West and North-East regions of the cluster, with the following proposal IDs: 60.A-9345(A) (PI: Caputi & Grillo) and 095.A-0653(A) (PI: Caputi)

We use a new reduction of the MUSE datacube, performed for the analysis of B24. To extend the redshift measurements, we use the complete redshift catalogue from the CLASH-VLT program (ESO ID: 186.A-0798; PI: P. Rosati) produced by [Mercurio et al. \(2021\)](#) within the BUFFALO footprint.

3 EXISTING MASS CONSTRAINTS

As we aim to disentangle DM from baryons, we need to gather several sets of constraints to probe the total mass as well as each baryonic component. In this section, we present the available datasets, which are taken from B24, and we will briefly recall how they were obtained. In Sect. 3.1, we describe the strong lensing sets that constrain the total mass, and in Sect. 3.2, we present the X-ray quantities used to probe the intra-cluster medium (ICM).

3.1 Lensing constraint

We constrain the total mass using strong gravitational lensing, in particular, multiple images. In this work, we use the same set of constraints as in B24; thus, we refer the reader to that work for a more detailed description. This set comprises the positions of 67 multiple images distributed over 25 systems. Each system has been confirmed spectroscopically; thus, we only use high-quality lensing constraints. The position of each image is presented in Fig. 1.

3.2 X-ray analysis

The B24 analysis provided the X-ray properties and associated maps of the ICM used in this work. This previous work provides full details regarding the methodology and analysis, which we briefly summarise here.

To model the ICM mass, we rely on its X-ray emission. We use a combination of surface brightness and spectral data. The former is accessed through maps of photon counts, while the latter provides the conversion factor from the surface brightness to the gas mass. We binned the cluster field with VORBIN python packages ([Cappellari & Copin 2003](#)) in the $[4, 7]$ keV band, with a signal-to-noise threshold of 10. For each of these cells, we extract the spectra. We fit them with the Astrophysical Plasma Emission Code (APEC)² model combined with a photoelectric-absorption (PHABS)³ model to account for the foreground galactic gas. Hence, we recovered the temperature and metallicity of the ICM, which allowed us to compute the conversion factor from photon counts to gas mass.

Our surface brightness estimation is based on the count maps in the soft, medium and hard energy *Chandra* science bands ([Evans et al. 2010](#)) that are combined with their associated exposure maps. To estimate the background emission, we recover the *blank-sky* observations associated with each observation.

² <http://atomdb.org/>

³ <https://heasarc.gsfc.nasa.gov/docs/xanadu/xspec/manual/XSmodelPhabs.html>

¹ <https://www.cosmos.esa.int/web/gaia/dr3>

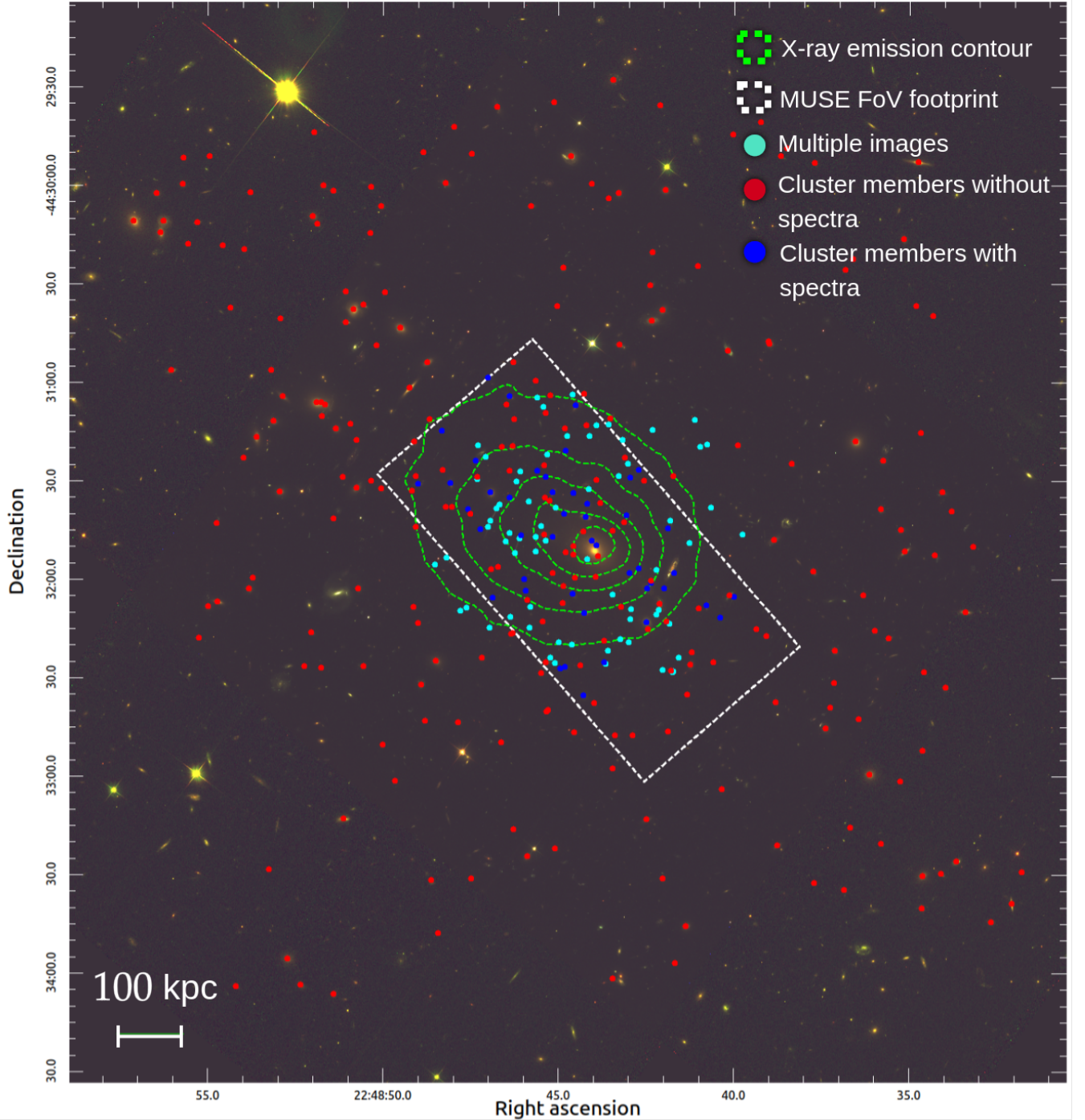


Figure 1. BUFFALO composite colour image of AS1063 with the following *HST* filters: F435W (blue), F606W (green) and F814W (red). The footprint of the combined MUSE observations is highlighted by the white dashed rectangle. The X-ray surface brightness from the CHANDRA X-RAY OBSERVATORY is shown by the green dashed contours. The set of multiple images used in this work is highlighted by the cyan dots. Red and blue dots present the spectroscopically confirmed cluster members, the latter colour indicating the availability of velocity dispersions measured from the MUSE datacube.

4 SUPPLEMENTARY MASS CONSTRAINT 1: CLUSTER MEMBERS

To model the cluster member mass distribution and, in particular, separate its baryonic and DM counterparts, we rely on photometric and spectroscopic measurements. To model the stellar mass distribution, we fit the light profiles with a method that we tailored towards

crowded fields such as galaxy clusters, presented in Sect. 4.1. Some of the parameters of these light profiles are also used in the modelling of their DM distribution. As the light profile provides a 2D representation, a missing key piece is the needed factor to scale such a profile to the DM and baryonic masses. We address this in Sect. 4.2 where we measure the line-of-sight velocity dispersions (LOSVD)

to probe the total mass, and in Sect. 4.3, where we recover stellar masses from spectral energy density (SED) fits.

All these measurements form the basis of our cluster member modelling, which is detailed in B25b (sections 2.2 and 3.3). In particular, section 2.2 presents the modelling assumptions used to define the cluster member DM and stellar mass distribution model. In section 3.3, we detail how we specifically constrain the cluster member total mass thanks to their stellar kinematics. We publicly release each of these measurements and some intermediary data products as presented in Sect. 6. For the cluster member, we provide light profile parameters, LOSVD and stellar mass estimates as well as the empirical Point Spread Function (PSF) and galaxy masks used in Sect. 4.1.

4.1 Light profiles

To improve the modelling of cluster member masses, particularly the modelling of their mass distribution with a baryonic and a DM component, we need to extract enough information to characterise the baryonic mass contribution. The simplest approximation of baryonic mass is to assume that it is proportional to the cluster members light distributions. Hence, in this section, we focus on extracting the light profile from imaging data.

In the following, we define cluster members as all objects which have a spectroscopic redshift in the $[0.30905, 0.3716]$ range, as measured by Mercurio et al. (2021) from the complete CLASH-VLT data on AS1063. We made the selection based on spectroscopic catalogues presented in Sect. 2.3. We do not consider photometrically selected cluster members, as the CLASH-VLT data cover the full FoV of the BUFFALO mosaic.

As cluster fields are particularly crowded, we need a method to extract light profiles while taking into account other galaxies in the field. Tortorelli et al. (2018) showed that light profile measurements done independently for each object have an increasing bias toward the cluster centre as the field becomes increasingly crowded. They relied on the MORPHFIT (Tortorelli & Mercurio 2023) method to perform 2D profile fitting in a cluster field. However, this method is not satisfactory for our goals as it does not provide profiles that can easily be included in lensing mass models, and it requires prohibitive computing costs. Hence, we developed our own method, which minimises the computing cost of such analysis and takes benefits from modern hardware accelerators such as GPU through the JAX python package (Bradbury et al. 2021). A scheme of the method workflow is presented in Fig. 2 and highlights the different steps of the process that we detail here: object detection (Sect. 4.1.1), region fit (Sect. 4.1.2) and individual Bayesian optimisation (Sect. 4.1.3). In particular, this method aims at measuring the profiles of cluster members only. However, we use the light model, including cluster and non-cluster galaxies, to extract the ICL light distribution through a separate analysis presented in Sect. 5.1.

4.1.1 Object detection and fitting setup

To set up our fitting process, use a similar approach as GALAPAGOS or MORPHFIT to detect objects by using SExtractor (Bertin & Arnouts 1996). Following a standard procedure, we start by performing a *hot* and *cold* pass to detect objects (Rix et al. 2004). We provide in Appendix A the SExtractor parameters that we use for this work. We concatenate the two catalogues by excluding hot components included in the KRON_RADIUS of the objects detected by the cold pass. In our particular case, we aim at measuring the profile

of galaxies in different bands; thus, we use the double image mode and choose as our base detection image the *HST* filter F105W. This filter provides a good balance between the depth and FoV of the BUFFALO data, as well as the number of detectable objects.

We are also relying on SExtractor to estimate the background emission. We here use the same parameters as the previous *hot* and *cold* passes, with the exception of BACK_SIZE parameters that we fix to 3096 pixels to smooth out the effect of the ICL. We cannot use the background produced by the two initial passes as a significant part of the ICL is included in it. With such a large BACK_SIZE, we limit the leaking of the ICL light distribution in the background estimation, but that set of parameters is not well-suited to detect objects in the image. Hence, we run SExtractor four times in total, a cold and a hot pass with the parameter presented in Appendix A, and we run again a cold and a hot pass with the large BACK_SIZE where we only aim at estimating the background. We define the final background that we use in the light profile fitting as the mean between the two SExtractor backgrounds provided by each pass with the large BACK_SIZE.

To estimate a PSF for each band of interest, we use a Principal Component Analysis (PCA) based method (Tortorelli & Mercurio 2023; Amara & Quanz 2012) similar to the one implemented in MORPHFIT. The more stars are included, the more accurate and complex such a PSF will be (Herbel et al. 2018). As an empirical method, it naturally accounts for effects due to the reduction of the raw data to the final mosaic, such as drizzling. In preliminary analysis, this method was superior to a stack of unsaturated stars once we used more than ~ 10 stars, as it presented fewer artefacts. To compute such PSF, we extract postage stamp images of unsaturated stars of size 4.2×4.2 arcsec, representing 70 pixels at the resolution of our drizzled images. These postage stamp images are then background-subtracted. We estimate the background using a sigma-clipped median of the postage stamp with a 5σ limit. We finish the preparation of the postage stamp images by normalising them. We perform a PCA decomposition as implemented in the SKIT-LEARN package (Pedregosa et al. 2011) on the array of the flattened postage stamp images. We select the number of PCA components by taking the minimal number of components, which explains 95 per cent of the data variance. We finish our estimation by subtracting the sigma-clipped median for the individual stamps and normalising the final PSF. We use a single PSF for the whole field. We manually select the unsaturated stars in each band in the field with the FLUX_RADIUS-MAG_AUTO plane where stars distinguish themselves as they present similar radii with varying magnitudes.

4.1.2 Region fit

To deal with the crowded field of the cluster, we start with a crude model of the BCG and the ICL using a Multi-Gaussian Expansion (MGE; Cappellari 2002) fit with the *MgeFit* python package. To capture the light distribution, Gaussians only share the same centre and are fitted on twisted isophotes. We restrict the fit to an ellipsoidal aperture following the position angle of the BCG as fitted by SExtractor and a major and minor axis of 150 kpc and 130 kpc, respectively. We voluntarily restrict this area to the whole extension of ICL in the cluster field, as our procedure includes only a simple estimation of the background. Hence, we preferred to focus on its brighter part, where the light profile estimation is the most robust. We mask all galaxies in this aperture. We find that the fit robustness is improved by removing the BCG and the ICL before fitting the other galaxies instead of accounting for them with elliptical profiles as in MORPHFIT.

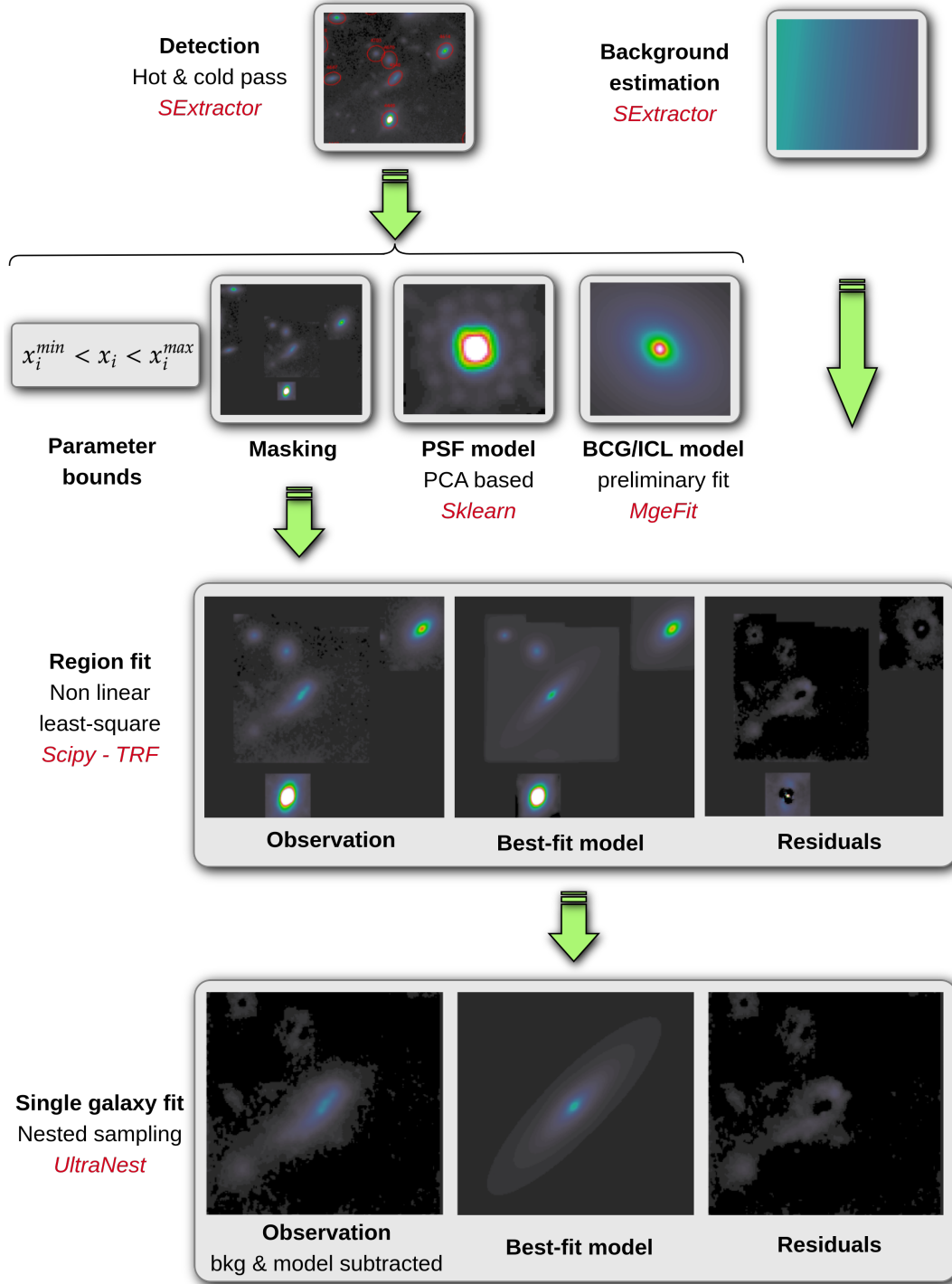


Figure 2. Diagram of the workflow to fit the cluster members light distribution. The first step is split between estimating the background and building the galaxy catalogue. We extract the necessary quantities from this step to proceed to the first fitting step: PSF estimation, masking, parameter bounds, and preliminary ICL estimation. The second step is based on fitting regions that include multiple galaxies. Regions are defined from the galaxy catalogue estimation of galaxy sizes. The final step consists of a Bayesian inference for each galaxy, where the influence of neighbouring objects is accounted for with the model computed in the previous step.

We continue our fitting procedure by defining the fitting regions. All galaxies are fitted (cluster members and other field galaxies) in a square based on a radius of four times their half-light radii, as estimated by FLUX_RADIUS measurements. We rescale FLUX_RADIUS values by $(1 - \epsilon)^{-1}$, with ϵ being the ellipticity

of the considered object. This is the equivalent of rescaling that radius to the major axis of the associated ellipse. It is comparable but slightly smaller than the value used by MORPHFIT as it considers a radius of five half-light radii instead (Tortorelli & Mercurio 2023). We define a region for each contiguous area of overlapping postage

stamps associated with individual galaxies. In addition to these regions, we manually mask objects such as stars and their flares as well as galaxies with morphologies too complex for a singular elliptical profile, such as lensing arcs. These manual masks are not applied to cluster members to ensure they are all included in the mass model.

For each object except the BCG, we either fit a dual Pseudo Isothermal Elliptical model (dPIE; Limousin et al. 2005) for cluster members or a Sérsic (Sérsic 1963) profile for field galaxies. That way, the dPIE light profiles can be added to the mass model easily, as a dPIE has an analytical expression for all its lensing quantities (Kassiola & Kovner 1993). We detail the specific treatment of the BCG and ICL in Sect. 5.1. They are fitted by a MGE. We re-parameterise these potentials to ease the numerical optimisation. The profile expressions with the re-parametrisation are detailed in Appendix B. We start by fitting separately each region with a non-linear least-squares fit. Once the model has begun to converge, we consider the influence of neighbouring objects from a separate region by performing another non-linear least square fit, where we subtract the global model from all other regions in the considered postage stamp. We perform these fits sequentially, such that the brightest postage stamp is fitted first. We define our sequence by weighting each region based on the luminosity of its object. We proceed by defining a Gaussian kernel density estimator with the galaxy positions in the whole field weighted by their magnitude, and we integrate this density in the region area to obtain the final weight.

Preliminary tests showed that applying the least square fit to the regular weighted residual $\frac{f_{\text{obs},i} - f_{\text{model},i}}{\sigma_i}$ is not the most efficient numerical function to minimise. In our case, the crowded environment and limitation of using a single elliptical profile per object lead to unsatisfactory fits on faint objects surrounded by bright neighbours. In such cases and with our parameter bounds, the best-fitting solution typically shows the faint objects with an elliptical bias. We mitigate this bias by transforming the data and model with the \sinh^{-1} function, and propagating the error with the transformation derivative. The \sinh^{-1} function transforms the values of all objects that span different orders of magnitude into a similar range, which balances the fit between each object. In principle, it is similar to using a Cauchy loss (Mlotshwa et al. 2023) or the transformation applied on the residuals by SourceXtractor++⁴ (Bertin et al. 2020). We choose to transform the data instead of the residual, as it is easier to have a homogeneous likelihood for the Bayesian step that follows. In particular, we do not have to estimate the parameter of the Cauchy distribution to turn the loss into a proper likelihood.

To consider flux variations inside a pixel, particularly near the galaxy centre, we oversample pixels. We define an area of 15 pixels around the centre of each fitted galaxy, where we are using an oversampling factor of 3. We define this region around each galaxy centre as measured by SExtractor. Thus, these regions are fixed during the entire optimisation. We use a large oversampling area to ensure the profile centre remains in that area during the optimisation.

We use the bounded version of the trust region reflective algorithm implemented in SciPy as our non-linear least square optimiser⁵. We translate the original code to the JAX framework to allow the code to run on hardware accelerators. We define the bounds and the starting points of each parameter based on SExtractor measurements. We present the details of this procedure in Appendix C. The optimiser

is run in each region for $250 \times [\text{Nb}_{\text{pot}}/2]$ steps where Nb_{pot} represents the number of profiles fitted simultaneously in the considered postage stamp during the separate fit. Then, when regions are fitted sequentially, we reduce that number to $50 \times [\text{Nb}_{\text{pot}}/2]$ for each of them.

4.1.3 Independent bayesian fit

To have a final estimation of the galaxy model, we use the Monte Carlo nested sampling algorithm MLFRIENDS (Buchner et al. 2014a; Buchner 2019) from the ULTRANEST⁶ package (Buchner 2021). By performing this optimisation galaxy per galaxy, we effectively neglect the correlation between parameters from different objects. However, for most of them, we expect these covariances to be lower than the ones between parameters of the same profile. That way, we can estimate our model posterior distribution while avoiding the curse of dimensionality.

We define the fitting regions with the same individual squares for each galaxy as in the previous step, but we are not merging them into larger postage stamps. We subtract the previously estimated global model and background sky in each region, which accounts for neighbouring objects. We also use the estimation of parameters to resize large bounds used in the first step for computational efficiency, which then serve as intervals for uniform priors. We use it only for parameters associated with profile normalisation or specific radii. We detail the approach in Appendix D. For other parameters, we found that using the estimation from the best-fitting solution does not lead to efficient priors. Hence, the sampling run on these individual stamps can be performed only with information from the previous step, thus in parallel.

Fig. 3 presents the results of our fitting procedure in the *HST* image considering the F160W filter. The top panel presents the *HST* image where the non-fitted areas are masked, the middle and bottom panels show the output model and residuals, respectively. Our procedure is able to capture globally the shapes of the fitted galaxies in the field of AS1063, as shown in the output model. However, residuals highlight the limitation of our approach and of the chosen galaxy model. We notice an overestimation of the flux around some galaxies in the residual maps, like the two objects highlighted by letters 'A' and 'B'. These galaxies exhibit a complex morphology with spiral features that cannot be accounted for by Sérsic or dPIE profiles. Many galaxies also exhibit an over/underestimation pattern in their central part or outskirts, though this pattern is weaker than observed in spiral galaxies. These galaxies may be more accurately fitted with two profiles accounting for a bulge-disk decomposition.

Regarding the residuals, we present their distribution weighted by the inverse of the data error in Fig. 4. As one can see, there is a bias in estimating the flux, i.e., the median of the weighted residuals is -0.071 as shown by the black dashed line, which indicates a slight overestimation of the observed flux. As this median is computed on the residuals divided by the observational uncertainty, we can deduce that this overestimation is small compared to that error, representing only 7.1 per cent. The width of the distribution is measured with the median absolute deviation (MAD), scaled to be equivalent to a Gaussian standard deviation. We obtain a value of 0.775. Hence, according to the MAD, our models capture galaxy profiles within the observational errors, as in the ideal case we expect a value of ~ 1 .

In the ideal case of a Gaussian likelihood, we would expect the residuals to follow a normal distribution. However, as a consequence

⁴ <https://astrorama.github.io/SourceXtractorPlusPlus/Model.html>

⁵ https://docs.scipy.org/doc/scipy/reference/generated/scipy.optimize.least_squares.html

⁶ <https://johannesbuchner.github.io/UltraNest/>

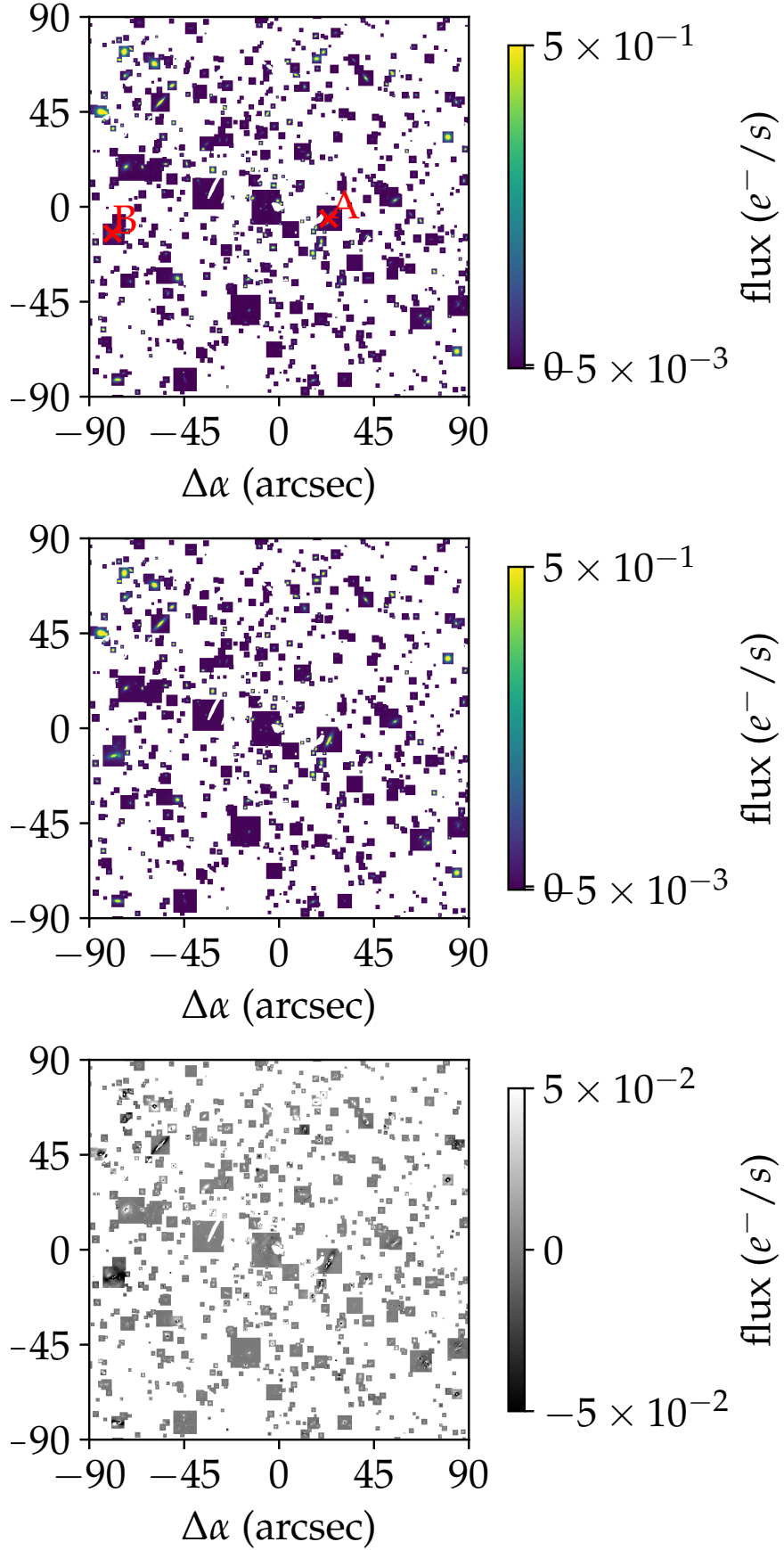


Figure 3. Region of $180'' \times 180''$ around the centre of AS1063: Original (top), model (middle) and residual (bottom) from the galaxy fitting procedure considering the F160W filter.

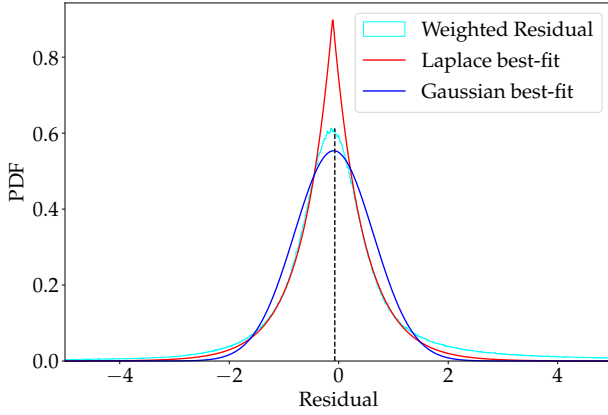


Figure 4. Distribution of the weighted residuals of the galaxy fit procedure for the filter F160W. This distribution is extracted from the masked area where galaxy fits are performed, and is presented with the cyan plain line. Plain red and blue lines represent the best-fitting results of a Laplace and Gaussian distribution. They highlight the broader tails of our residual distribution compared to a Gaussian distribution. These fits are performed with the weighted residual in the $[-2, 2]$ range. The dashed black line shows the median of the weighted residuals.

of our fitting procedure and likelihood choices, the residuals distribution slightly differs as one can see in Fig. 4. We overlaid the best-fitting results of residuals by a Laplace and a Gaussian distribution. We restrict the dataset to the $[-2, 2]$ range for both fits, yielding better results as the distribution contains outliers. Our distribution presents a narrower width but larger tails than a Gaussian distribution, which we would expect. The Laplace distribution is a more adequate fit as its width and tail agree better with the data. Indeed, if we except the mode of the residual distribution (i.e. $[-0.35, 0.15]$), which is badly reproduced by both distributions, in the $[-3, 3]$ range the Laplace distribution reproduce the residual density with a median absolute error of 16 per cent while the Gaussian one has an error of 46 per cent. Compared to the Gaussian, the Laplace distribution allows for more outliers than we expect from the simple model chosen for each galaxy model. It thus supports our likelihood choice, as it is the intended effect.

4.2 Line-of-sight velocity dispersions

To probe the cluster member total mass, we use the line-of-sight velocity dispersions (LOSVD), which can be expressed through their light and mass distributions (see B25b, section 3.3). For this task, we use the same method as in B24 with the MUSE datacube presented in Sect. 2.3, which we briefly describe in this section. In contrast to B24, we use our own measurement of the cluster member light profile to define extraction regions of the spectra, where we use dPIE instead of Sérsic profiles.

Galaxy spectra are extracted in elliptical apertures of circularised radius, R_e (i.e. half-light radius). Ellipticity and R_e estimations are based on dPIE fits performed in Sect. 4.1 using the F160W image. We used the Python package MPDAF (Bacon et al. 2016) to extract spectra, which uses an optimal extraction algorithm for CCD spectroscopy (Horne 1986). We use the estimation of the local background from MPDAF, which we subtract from the galaxy spectra. These spectra are restricted to 485 nm–716 nm in the observer frame, similarly to (Bergamini et al. 2019). We exclude the reddest part of

the MUSE wavelength range as it presents a lower S/N due to the MUSE sensitivity curve, and is affected by stronger sky subtraction residuals.

The LOSVD measurements are done with the python package pPXF (Cappellari 2017) combined with the nested sampling engine pyMultiNest (Feroz et al. 2019; Buchner et al. 2014b) as the non-linear optimiser method. To model spectra, we use spectral templates from the Indo-US Library of Coudé Feed Stellar Spectra (Valdes et al. 2004), which have a full width half maximum (FWHM) of 1.35 Å, and a pixel-scale of 0.44 Å pixel⁻¹. We parametrize the galaxy kinematics with the velocity, V , the velocity dispersion, σ_e , and the first two Hermite moments, (h_3 , h_4). We add a multiplicative Legendre polynomial of degree 3 to improve the continuum. The reliability of this pPXF configuration has been tested in B24 with 10000 mock spectra with a stellar population and observational noise tuned to represent AS1063 observations.

The optimisation is done in two steps. We start by a fit with a Trust Region Reflective algorithm implemented in SciPy (Virtanen et al. 2020) to detect outlier points automatically. We mask these points during the nested sampling runs, providing us with the final estimation of σ_e . We apply the polynomial correction defined in Appendix B from B24 with the updated coefficients presented in Beauchesne et al. (2025). We use these fits to constrain the cluster members scaling relations, for which we add a scatter to represent the inability of such a relation to reproduce exactly each galaxy properties. Hence, we do not rescale the error to include systematics, however, we include it in the overall scatter of the relation. On average, this scatter is one order of magnitude larger than the total error of σ_e .

4.3 Stellar masses

To be able to successfully disentangle baryons and DM contents in cluster members, we need insights on their stellar masses. Indeed, stellar kinematics is sensitive to the light distribution and total mass but not directly to the stellar-mass-to-light ratio ($Y_* = M_*/L$). To obtain such measurements, we fit the SED of cluster galaxies. However, to account for biases in the SED fitting, we use three different SED models. We use the computing service proposed by GAZPAR⁷ operated by CeSAM-LAM and IAP, to run the software LePHARE (Arnouts et al. 2013) with the SED model presented in Ilbert et al. (2015). The SED model is based on the stellar library presented in Bruzual & Charlot (2003), the Chabrier (2003) Initial Mass Function (IMF), and as a star formation history (SFH), a combination of two delayed-tau models and an exponentially declining model. In addition, we use the Python package BAGPIPES (Carnall et al. 2018, 2019) with two similar SED models with a different SFH. Both models use the stellar population model from the 2016 updated version of the Bruzual & Charlot (2003) models using the MILES stellar spectral library (Falcón-Barroso et al. 2011). The IMF is based on Kroupa (2001), and we assume a dust attenuation based on the Calzetti law (Calzetti et al. 2000). We use the same parametrisation as Carnall et al. (2018) for the nebular emission. For the SFH model, we use a delayed-tau SFH model or a double power-law parametrisation. For the BAGPIPES models, the SED model priors are presented in Table 1. We note that the IMFs of LePHARE and BAGPIPES are slightly different, with the Kroupa (2001) IMF providing stellar mass estimates 6 per cent higher than Chabrier (2003) ones (e.g. Speagle et al. 2014). However, that difference is negligible in our case as it is well domi-

⁷ <https://gazpar.lam.fr/home>

nated by the measurement uncertainties, which have a mode around 30 per cent of error for the three SED configurations.

To perform the cluster members SED fits, we rely on the aperture photometry measured by *SEXTRACTOR* in the seven HST filters: F435W, F606W, F814W, F105W, F125W, F140W and F160W. As not all bands have the same FoV, we do not have photometry for all galaxies in all bands, particularly as their distances to the centre increase. In preliminary tests, we try to use the photometry from the dPIE light model fit presented in Sect. 4.1.1. Unfortunately, although our light model procedure can provide a good best-fitting solution for all cluster members, including the faintest ones, the photometric uncertainties on these faint objects are particularly large, up to three orders of magnitude more than the fitted flux on some bands. Consequently, these large uncertainties produce wide posteriors for the stellar masses, which leads to unrealistic values for the median stellar masses that we will use in the mass models.

Fig. 5 presents cluster members stellar mass estimates as a function of their apparent magnitudes in the F160W filter. Apart from a few outliers, the three different SED models provide similar values within the expected systematic difference of SED fitting methods (Conroy 2013, i.e. < 0.3 dex). One can notice systematic differences between models for the fainter end of the cluster member distribution. The SED with a double power-law SFH provides the highest stellar masses, while *LePHARE* gives the lowest. Stellar masses estimated by the SED model with the delayed SFH are located between the two other models. As these differences of a few tenths of dex are expected for different SED fit methods, we keep the three estimates to understand the resulting biases on the lensing mass models. Indeed, the median of stellar mass estimates is used to define the baryonic content of each cluster member, as it is presented in B25b, section 2.2.

5 SUPPLEMENTARY MASS CONSTRAINTS 2: BCG & ICL

Similarly to cluster members, we rely on the same measurements to constrain the BCG and the ICL stellar mass through light distribution (Sect. 5.1) and stellar masses (Sect. 5.3). We also recover the stellar kinematics, although in that case, it is probing the cluster total mass distribution and not only the BCG one. In particular, the light distribution will serve as a starting point for the modelling of the mass of the BCG and the ICL component, which is presented in B25b, section 2.3.

Thanks to the spatial extension and high signal-to-noise in the BCG and ICL spectra, we rely on a refined kinematic model through the JAM package, which requires the second moment of the velocity along the line-of-sight (LOS) axis, V_{rms} , instead of the LOSVD. We detail how we extract the V_{rms} in Sect. 5.2. This measurement allows us to define a new likelihood which complements the strong lensing observations in the very centre of the cluster. It is presented in B25b, section 3.4.

Similarly to the cluster members, we make the measurements presented in the next sections publicly available, through the repository given in Sect. 6. In particular, we provide the MGE parameters in the different bands, V_{rms} and stellar mass estimates, as well as the extraction masks used for the kinematics measurement.

5.1 Light distribution

Several works have extracted the ICL profile from imaging data, including in AS1063 (e.g. Montes & Trujillo 2018). Different methodologies have been utilised, such as composite model including mul-

tipole Sérsic profiles (Janowiecki et al. 2010), "wavelet-like" decomposition (Da Rocha & Mendes de Oliveira 2005; Jiménez-Teja & Dupke 2016; Ellien et al. 2021) or methods taking advantage of 2D fitting algorithms used to measure galaxy light profiles (Giallongo et al. 2014; Morishita et al. 2017). In the present case, we also want to constrain the stellar kinematics. Hence, we follow the composite model approach with a MGE model. Such parametrisation has been used extensively to model galaxy stellar kinematics, assuming an axisymmetric light and mass distribution. In particular, we want to use the Jeans Anisotropic Modelling (JAM; Cappellari 2008) which is a computationally efficient way to compute the stellar kinematics for models that do not assume spherically symmetric distributions.

To recover the BCG and ICL light distributions, we follow the procedure presented in Fig. 6. We use the galaxy light profiles obtained in Sect. 4 to remove galaxies in the cluster field, and isolate the BCG and the ICL light emission in the F160W filter. As a single elliptical profile does not perfectly fit the galaxies in the core, we also mask their residuals, e.g., spiral arms. We also mask background objects. We then restrict the fitting regions to the same ellipsoidal aperture used in Sect. 4.1.2 for the preliminary BCG and ICL models. It is a fine-tuned version of the preliminary fit, as we are taking into account the flux of field galaxies instead of simply masking them to improve the robustness of the MGE fit.

We are interested in the best fit possible for the mass model (i.e. Twisted MGE) and an axisymmetric solution to be able to use JAM for the BCG and the ICL kinematics (i.e. Normal MGE). For the former, we use a MGE solution where each Gaussian is allowed to have a different position angle and is fitted on twisted isophotes, therefore a twisted MGE. Such parametrisation is well-suited for the BCG and ICL light distributions as it is expected that ellipticity and position angle will vary between the BCG and the ICL (Kluge et al. 2020). The axisymmetric MGE is fitted on ellipsoidal isophotes, and each Gaussian shares the same centre and position angle. This MGE will only be used to weight the mass in the kinematic computation, so it is less important to have the best 2D model. We enforce the weights of the Gaussian to be positive in both cases, even if negative weights allow for a better fit of the data. In particular, it enables us to split the MGE model into multiple MGE models, allowing for a varying stellar mass-to-light ratio, as presented in B25b, in section 2.3. To estimate the fit uncertainties, we rely on the JAX package and its automatic gradient computation to recover the Hessian of the mean squared error. We invert that Hessian and use the closest positive semi-definite matrix as the covariance matrix, following the property of the Fisher information matrix at the maximum likelihood. As we perform spectral energy distribution (SED) fits based on this MGE light model in Sect. 5.3, we are adding a systematic uncertainty of 5 per cent to homogenise the photometry among the different depths of each *HST* band.

The fitting results are presented in Figs. 7 and 8. Fig. 7 presents the masked image, the model fitted on twisted isophotes and the associated residuals. Fig. 8 presents the model and residuals for the normal MGE. Both profiles recover the global shape of the BCG and the ICL, though the axisymmetric fit exhibits a slightly worse orientation pattern. In particular, the twisted MGE presents a varying position angle and ellipticity with radius, as expected from this component. The ellipticity of the isophotes increases with the radius. For the normal MGE fit, we also observe the same ellipticity behaviour to a lesser extent.

Regarding the amplitude of the residuals, we gather the distribution of residuals weighted by the data errors. The twisted MGE fit presents a median and a scaled MAD of 0.037 and 1.111 in the fitting area, respectively. On the other hand, the axisymmetric MGE has -0.007

Table 1. Priors of the SED model parameters used by BAGPIPES. \mathcal{N} , \mathcal{U} , $\mathcal{N}_{\text{trunc}}(a, b)$ refers to a normal, uniform and truncated normal distribution with a and b the bounds of the truncated normal. For \mathcal{N} and $\mathcal{N}_{\text{trunc}}(a, b)$, prior parameters correspond to the mean and standard deviation of the distribution, while for \mathcal{U} , it is its bounds.

Parameter	Prior parameters	Prior type
Redshift	$(z_{\text{measured}}, 0.001)$	\mathcal{N}
Log stellar mass formed	$(1, 15) \log M_{\odot}$	\mathcal{U}
stellar metallicity	$(0, 2.5) Z_{\odot}$	\mathcal{U}
V-band attenuation	$(0, 2.) \text{ mag}$	\mathcal{U}
Age since formation	$(0.1, t(z_{\text{obs}})) \text{ Gyr}$	\mathcal{U}
Delayed SFH: τ	$(0.3, 10) \text{ Gyr}$	\mathcal{U}
Double Power-law SFH: τ	$(0., 15) \text{ Gyr}$	\mathcal{U}
Double Power-law SFH: $\log_{10} \alpha$	$(-2, 3)$	\mathcal{U}
Double Power-law SFH: $\log_{10} \beta$	$(-2, 3)$	\mathcal{U}
Calibration: $\log_{10} \sigma_e$	$(2.30, 2.84) \log_{10} \text{ km/s}$	\mathcal{U}
Calibration: P_0	$(1, 0.25)$	$\mathcal{N}_{\text{trunc}}(0.5, 2.5)$
Calibration: P_1	$(0, 0.25)$	$\mathcal{N}_{\text{trunc}}(-0.5, 0.5)$
Calibration: P_2	$(0, 0.25)$	$\mathcal{N}_{\text{trunc}}(-0.5, 0.5)$
White noise: $\log_{10} \text{ scaling}$	$(0, 1.70)$	\mathcal{U}

and 1.319 for the same statistical indicator. Hence, both of these fits present a bias similar to or inferior to the global fit (i.e. -0.071), which is expected as the areas of bad fit have been mostly masked. As anticipated, the twisted MGE provides a better fit of the data with a MAD estimation 20 per cent smaller than the normal MGE parametrisation. However, both fits represent the data well, as the estimate of their scaled MAD is close to 1.

Finally, we convert the light distribution to a mass distribution with the mass-to-light ratio of the Sun ($M_{\text{R, AB}} = 4.60$) in the R-band from Willmer (2018). We use this mass distribution to compute the associated lensing potential by fast Fourier transform, and we obtain the other lensing quantities by deriving this potential. These quantities can then be rescaled with the stellar mass-to-light ratio of the BCG and the ICL in units of the Sun mass-to-light ratio to match the correct mass. As Montes & Trujillo (2014) and Montes & Trujillo (2018) found a gradient of colour and metallicity with radius in HFF clusters, implying a varying mass-to-light ratio, we split the MGE parametrisation into multiple MGE models. Each of these MGE models has a distinct mass-to-light ratio, which allows for a variation of the mass-to-light ratio of the whole component, the flexibility of which depends on the number of MGE models considered. The case of maximal flexibility, which is one MGE model per Gaussian function used in the overall representation, follows the approach presented by Collett et al. (2018).

5.2 V_{rms}

To measure the evolution of V_{rms} as a function of the radius, we extract the BCG and the ICL MUSE spectra in increasing elliptical annuli. We fix the extraction centre coordinates, position angle and ellipticity to the same ones as the elliptical isophotes defined to fit the associated light distribution in Sect. 5.1. For consistency with the kinematic constraints and their use with the JAM library, we use the normal MGE fit (i.e. axisymmetric) as the basis for the extraction region. We use the white MUSE light and the HST images to mask galaxies present in the extraction area. The widths of the annuli are defined iteratively by increasing their radii by the size of the MUSE PSF until

the associated spectrum has a median signal-to-noise, S/N , above a threshold of 5. As the MUSE data were taken without adaptive optics correction, we assume that the MUSE PSF width is approximately the seeing of the observation (i.e. ~ 1 arcsec). This estimation is consistent with the PSF FWHM measured during the data reduction. We limit the radius of the aperture to 100 kpc, which leads to 14 regions. We use the same procedure for the ICL as the one for the galaxies, except that we do not remove the local background. The estimate of this background by MPDAF misidentifies the ICL as the background sky, which tends to modify the shapes of the spectra. The fit on the last two regions failed as the spectra are too noisy, leaving us with 12 data points. In those 12 points, the last two points do not follow the same pattern as the previous ones, with a high variability between them. Indeed, the last three points present σ_e of 461, 394, and 574 km/s, thus we reject these last two data points as they appear to be dominated by systematic error, reducing our final dataset to 10 points. The whole V_{rms} measurement set is presented in the top panel of Fig. 9, including the last four rejected data points.

As presented in Sect. 4.2, our procedure allows us to measure V and σ_e , which are linked to V_{rms} such that $V_{\text{rms}} = \sqrt{V^2 + \sigma_e^2}$. Hence, we use the same fitting procedure here, including the polynomial correction. As we are directly fitting these data, we rescale the error by the underestimation factor found in Beauchesne et al. (2025), which is 1.33. This underestimation bias has been estimated by using this fitting procedure on 10000 mock MUSE spectra. The mocks were designed to present similar stellar populations and observational uncertainties as the cluster members in AS1063. In Fig. 9, we present the masked white MUSE images and the extraction regions with their best-fitting V_{rms} . As shown in this plot, the V_{rms} increases as we move from the kinematics of the BCG (i.e. the two most inner extraction regions) to the ICL, as seen in local clusters (e.g. Longobardi et al. 2018). The V_{rms} values range from ≈ 341 km/s in the BCG to 465 km/s in the elliptical bin with maximum radii.

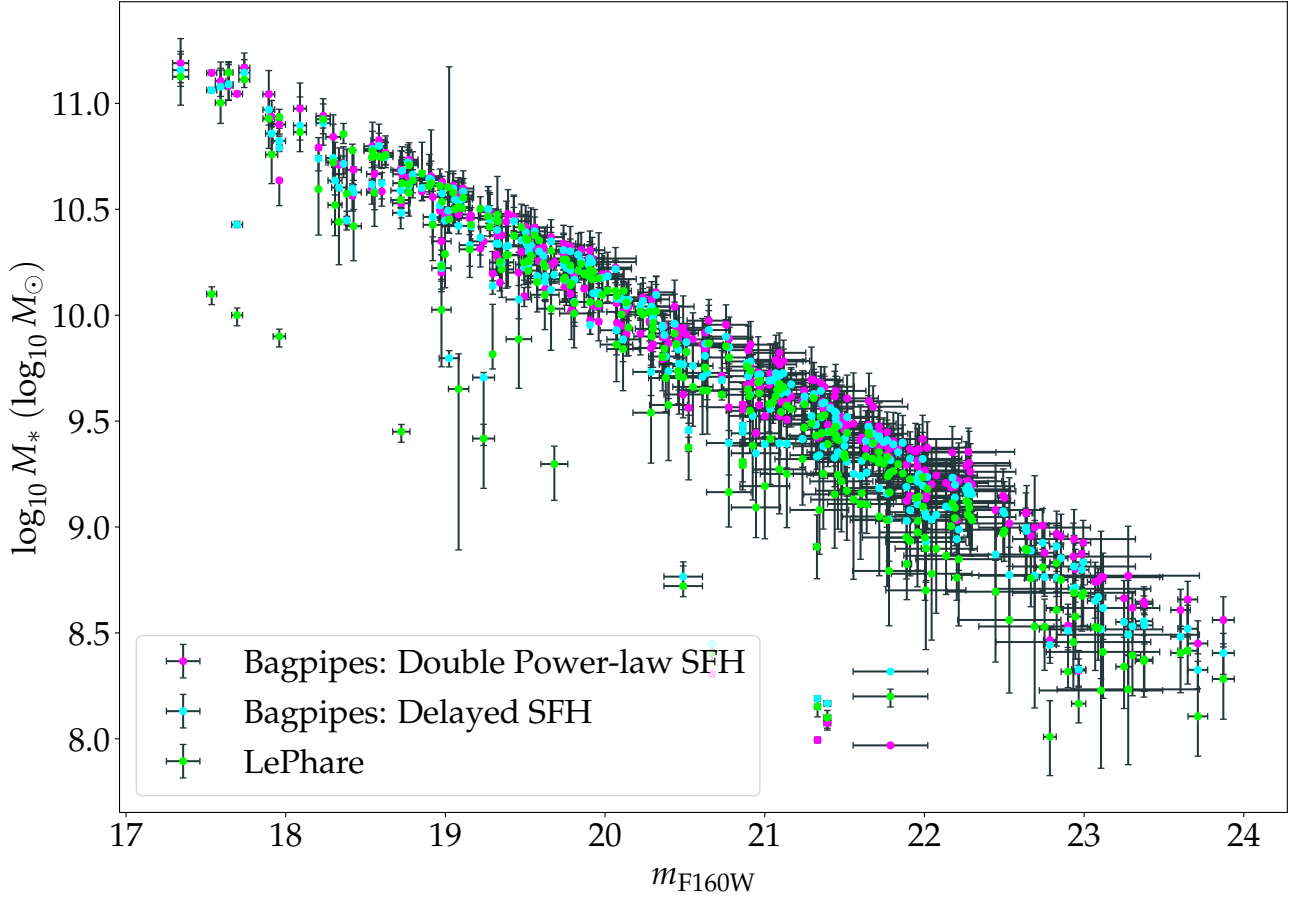


Figure 5. Cluster member stellar masses (M_*) as a function of their apparent magnitude in the F160W filter (m_{F160W}). Error bars on M_* present the 1σ credible interval from the SED posterior parameters while representing the standard deviation for F160W. The magenta, cyan, and lime coloured dots represent the stellar mass estimates provided by BAGPIPES with a double power-law SFH, BAGPIPES with a delayed SFH, and LEPHARE, respectively.

5.3 Stellar masses

For the BCG and the ICL components, as we use the spectroscopic information provided by the MUSE data, we extract their photometry in each elliptical annulus where we measure the stellar kinematics. We measure the photometry by reproducing the procedure described in Sect. 5.1 for F435W, F606W, F814W, F105W, F125W and F140W filters, which gives us MGE light models of the BCG and the ICL components. When considering LEPHARE, only the broadband filter photometry is used to constrain the SED model. In contrast, the two BAGPIPES settings rely on combining photometric and spectroscopic data. To account for any miscalibration between photometry and spectroscopy, we follow the approach of Carnall et al. (2019), and add second-order Chebyshev polynomials as a multiplicative function of the spectra and a Gaussian white noise model. Priors used for the polynomials and white noise are listed in Table 1.

Fig. 10 presents the stellar-mass-to-light ratio Υ_*^{BCG} of the BCG and the ICL components in the F814W (top panel) and F160W bands (bottom panel) filters. For both filters, we normalise the luminosity by the sun luminosity ($M_{R,AB} = 4.60$) in the R-band from Willmer (2018). Both BAGPIPES SED models provide similar stellar mass estimates, with all data points agreeing with one standard deviation except the second and third ones. In contrast, LEPHARE prefers a

slightly larger estimate of the stellar mass but with larger uncertainty such that it agrees with the BAGPIPES models within two standard deviations on all data points. It is opposite to the pattern seen in Fig. 5, as cluster member stellar masses estimated by LEPHARE are lower. This difference is likely due to the inclusion of the MUSE spectra for the SED fit of the BCG and the ICL. When BAGPIPES was run with photometry only in preliminary tests, its stellar mass estimates were much closer to the output of LEPHARE. Although stellar mass estimates obtained by combining spectroscopic and photometric data are within the 3σ CI of the photometry-only runs. Hence, all SED models provide similar estimates of the BCG and the ICL stellar masses.

From these SED fits, we obtain an estimate of the stellar mass of the BCG and the ICL components. By combining all elliptical bins considered in Fig. 10, we obtain 6.83 ± 0.17 , 7.20 ± 0.11 and $8.98 \pm 0.34 \times 10^{11} M_\odot$ for the fits with a delayed SFH, a double power-law SFH and the LEPHARE SED models, respectively. Assuming that all bins within the half-light radius of the BCG are a good representation of its stellar mass (i.e. the four most central bins), we obtain for the fits with a delayed SFH, a double power-law SFH and the LEPHARE SED, a stellar mass of 3.15 ± 0.21 , 3.45 ± 0.12 and $4.05 \pm 0.51 \times 10^{11} M_\odot$, respectively. Hence, the BCG would

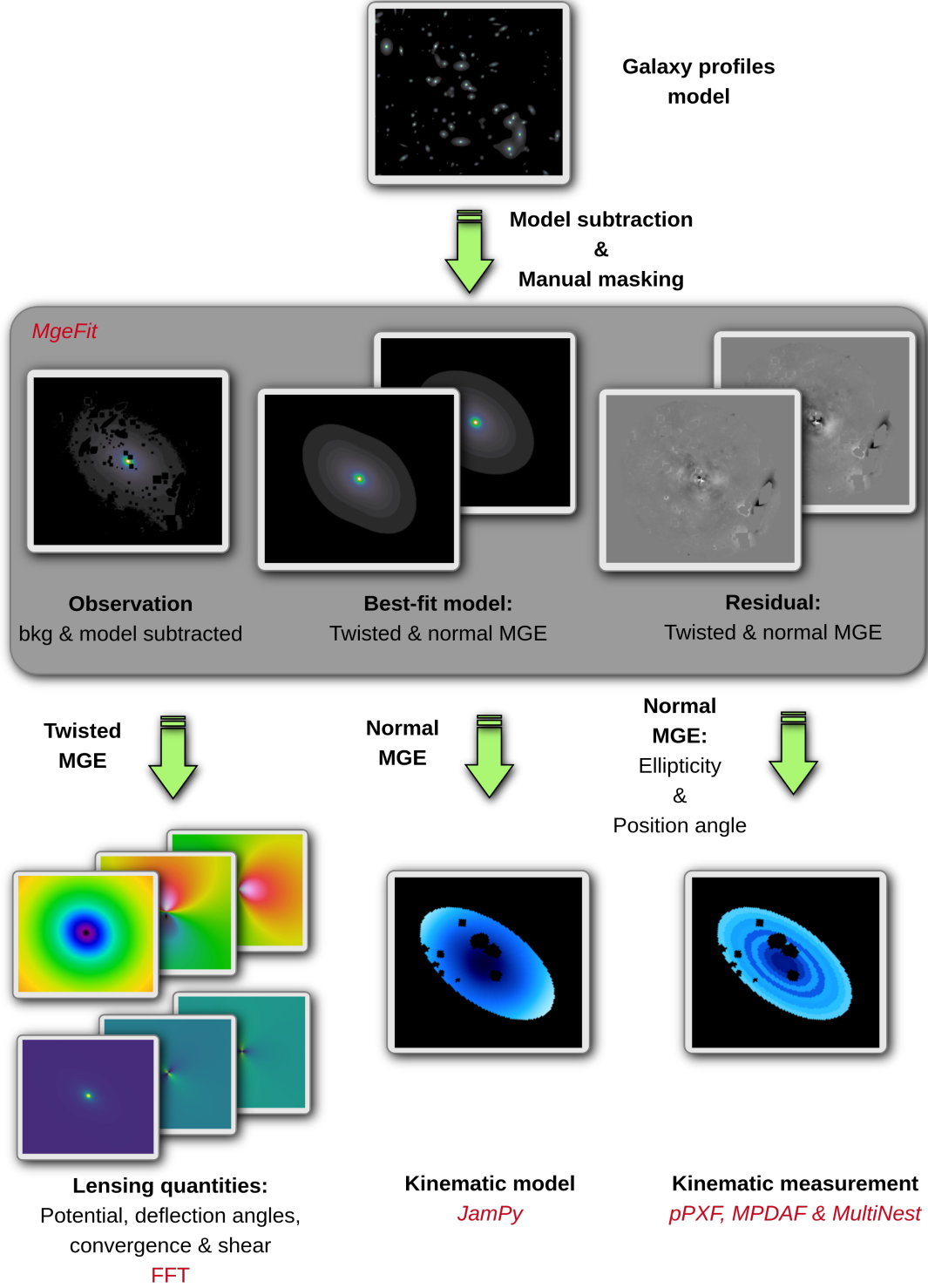


Figure 6. Diagram of the workflow to extract the BCG and the ICL kinematics, and their light distributions. The light distribution is estimated in the data image, where light profiles of galaxies have been removed. We made this estimation with MGE fits, using two parametrisations: an axisymmetric and a concentric. We define the extraction regions for the kinematics fit and estimate the lensing quantities based on the MGE light profiles.

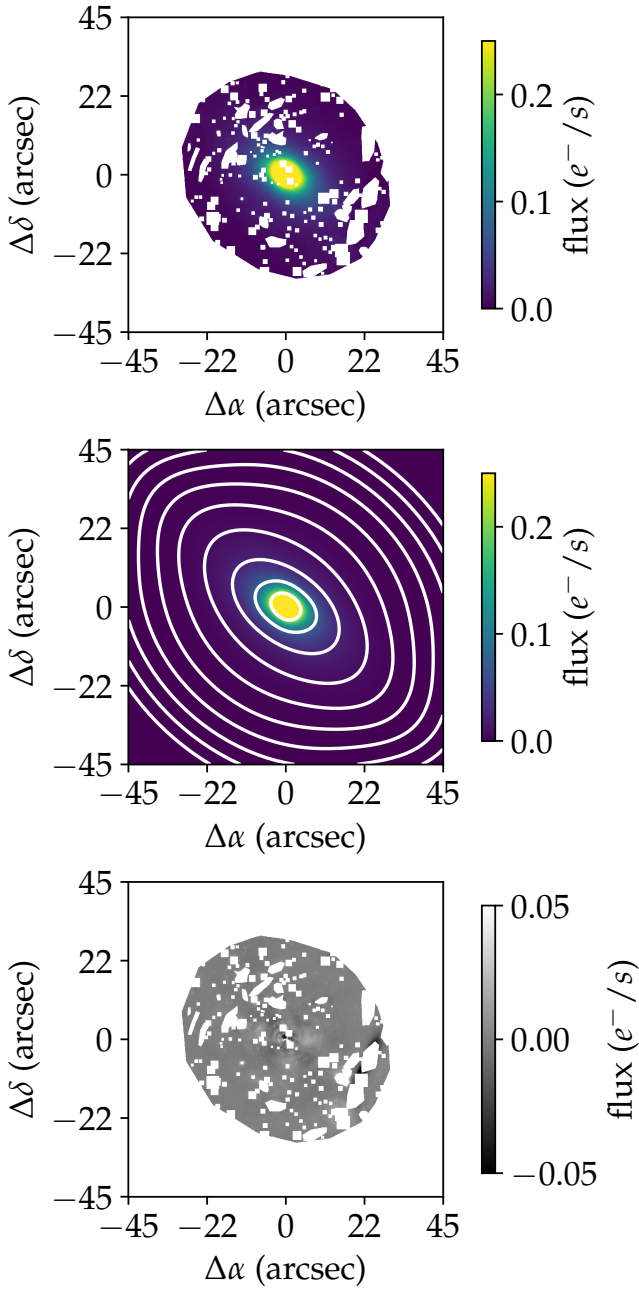


Figure 7. From top to bottom: Masked *HST* image in the F160W filter where all galaxy models have been subtracted, best-fitting MGE model on twisted isophotes and associated residuals

account for roughly half of the stellar mass of the BCG and the ICL components.

Regarding a possible gradient in $\Upsilon_{*}^{\text{BCG}}$, the radial variation is limited in both F814W and F160W filters. The variation between the data points is mostly within the statistical uncertainties. The BAGPIPES SED models present a decrease of $\Upsilon_{*}^{\text{BCG}}$ with the radius, followed by an increase over the last two data points. However, according to the statistical uncertainties, most of these points agree with a constant $\Upsilon_{*}^{\text{BCG}}$ within two standard deviations. This pattern disagrees with LEPHARE, which does not show significant variations with the distance from the cluster centre. Variations of $\Upsilon_{*}^{\text{BCG}}$ are smaller in the

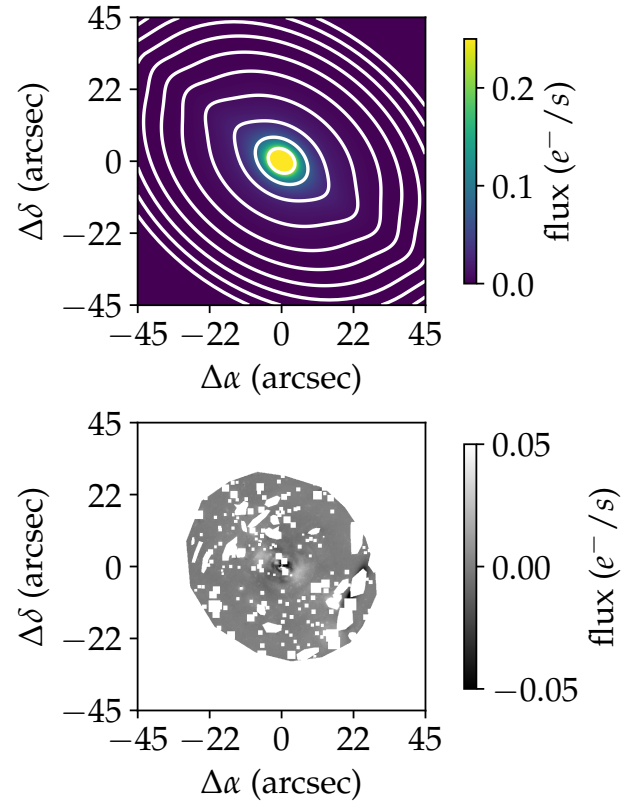


Figure 8. best-fitting MGE model with an axisymmetric parametrisation (top) and associated residuals (bottom).

F160W filter. When all SED models and data points are combined, we obtain $\Upsilon_{*}^{\text{BCG, F160W}} = 8.57 \pm 1.42 M_{\odot}/L_{\odot, R}$ in comparison to $\Upsilon_{*}^{\text{BCG, F814W}} = 11.57 \pm 1.90 M_{\odot}/L_{\odot, R}$. Hence, there is ≈ 30 per cent more dispersion in the F814W than in F160W filters, which favours the use of light distribution in F160W as a tracer of the stellar mass to model the baryonic content of the BCG and the ICL.

As reported by Xie et al. (2024) from radio observations, there is likely an active galactic nucleus (AGN) in the BCG. To test possible bias in the estimated stellar masses, we try to add an AGN component to the BAGPIPES SED models, similar to the one used by Carnall et al. (2023). We fit the most central bin with this extended model, which leads to a variation of less than 1 per cent of the median of the stellar mass posterior. Hence, we consider that the bias due to the possible presence of an AGN is negligible in our case, although the considered wavelength range is mostly dominated by stellar emission, which may bias this check. Indeed, for the SED best-fitting solution with an AGN component, the AGN emission significantly dominates the overall one for wavelengths superior to $\approx 3.15 \mu\text{m}$.

6 CONCLUSION

In the first paper of this series, we focus on the required analysis of the observational dataset to extract constraints for a comprehensive mass modelling of AS1063. In particular, we present the existing mass constraints in the form of strong lensing and X-ray observations, which provide no knowledge on the stellar mass contained in cluster members, the BCG and the ICL. We then detail specific methodologies based on photometric and spectroscopic data to recover the light

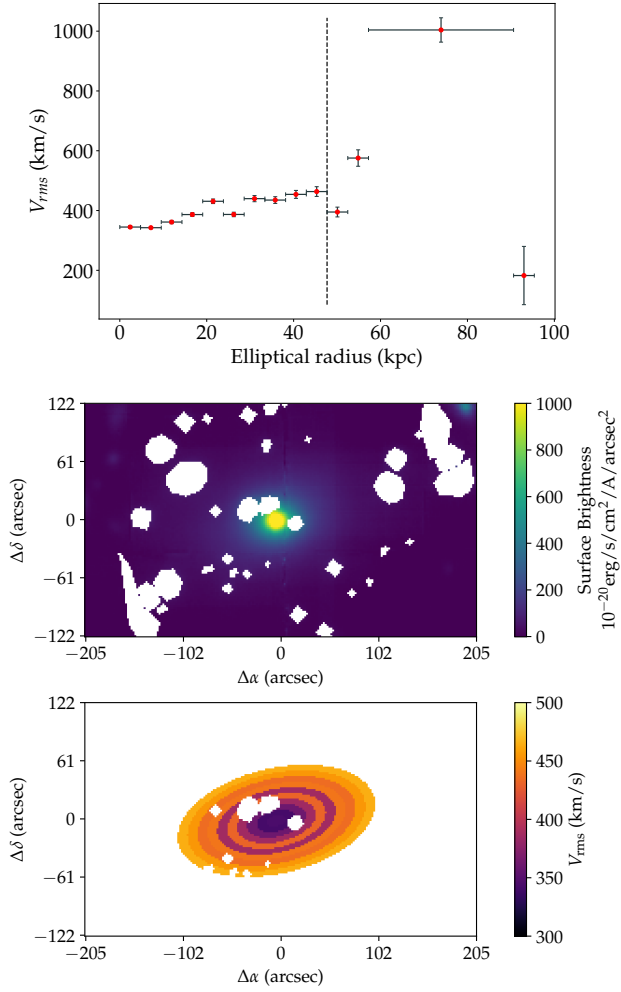


Figure 9. Kinematic estimation of the BCG & ICL. *Top panel:* V_{rms} estimate as a function of the elliptical radius used to define the elliptical bins. *Middle panel:* Masked white image of the MUSE datacube. *Bottom panel:* V_{rms} estimate in each elliptical extraction region without the rejected data points.

distribution, stellar kinematics and stellar mass estimate of those components.

For cluster members, we begin by describing our procedure for recovering their light profiles, while accounting for neighbouring galaxies, in Sect. 4.1. Our approach consists of three main steps: detection (Sect. 4.1.1), region fitting (Sect. 4.1.2), and single-object fitting (Sect. 4.1.3). We use a standard detection procedure with cold and hot *SExtractor* passes. Based on these results, we identify contiguous regions where all objects are fitted simultaneously to obtain an estimate of the light profile maximum likelihood. We then finish our procedure by fitting individually each object with a nested sampling algorithm, where the neighbouring objects are subtracted based on the previous region fit. This method allows us to fit thousands of objects in a crowded field with a moderate computing cost. We then estimate their stellar kinematics through their LOSVD from the MUSE datacube (Sect. 4.2) and their stellar mass based on *SExtractor* aperture photometry using the available HST bands (Sect. 4.3).

For the BCG and the ICL component, we fit the light distribution with an MGE profile that benefits from the cluster member light

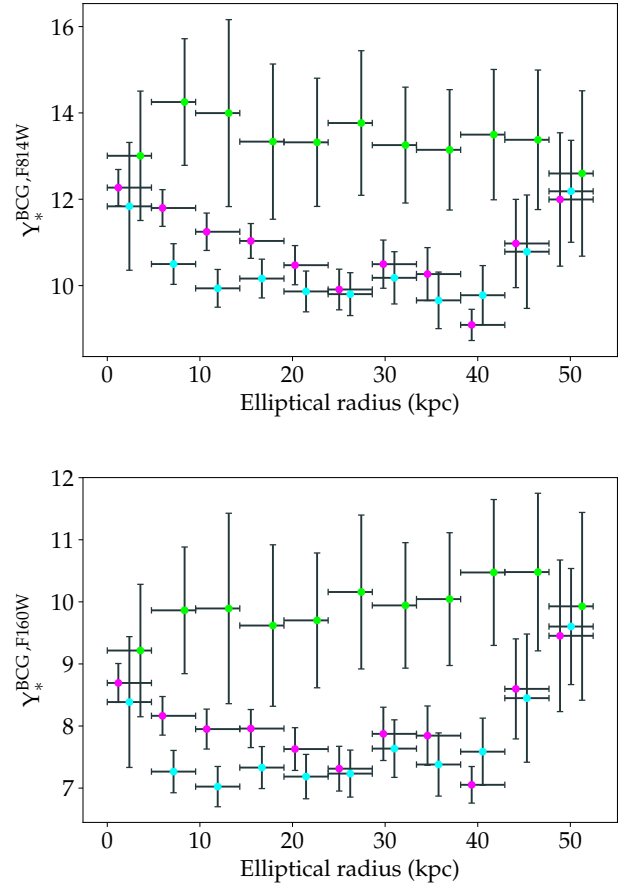


Figure 10. *Top panel:* Stellar-mass-to-light-ratio Y_{*}^{BCG} of the BCG and the ICL components in the F814W filter. The luminosity has been normalised by the solar luminosity in the R-band from Willmer (2018). Error bars represent standard deviations on Y_{*}^{BCG} made by propagating the error on the stellar mass and photometry, while the radius error represents the width of the extraction regions. To improve the readability of the plot, the results of each SED code have been slightly shifted horizontally. The magenta and cyan dots are associated with the BAGPIPES SED models with a double power-law and delayed SFHs, respectively. The lime-coloured dots represent the results obtained with LePHARE. *Bottom panel:* Same as the top panel for the F160W filter.

profile model, which is subtracted from the original datasets. We reproduce that measurement in each HST band to obtain the colour information required for the SED fitting. The light profile extraction is detailed in Sect. 5.1. Similarly to cluster members, we obtain the stellar kinematics through their V_{rms} within elliptical bins (Sect. 5.2) and their stellar mass by fitting their SED through their HST model photometry and MUSE spectra (Sect. 5.3).

The primary use of these analyses is the parametrisation of the mass model presented in B25b. In particular, we are using the light profile as a tracer of the stellar mass. We present our modelling assumptions in B25b, section 2, for all components. Thanks to the stellar kinematics measurements, we are able to add two new likelihoods to the approach of B24, which are described in B25b, section 3. The first likelihood uses a JAM kinematic modelling combined with the V_{rms} measurements to probe the cluster total mass down to inside the BCG. The second one constrains the cluster member total mass based on their LOSVD, which is computed with the light profile measured in this analysis, as well as their mass distribution.

ACKNOWLEDGEMENTS

The authors thank Massimo Meneghetti, Raphaël Gavazzi, Michaela Hirschmann, and Mireia Montes for their helpful discussions at various stages of the project. The computations were performed at the University of Geneva using Yggdrasil and Boabab HPC services. BB acknowledges the Swiss National Science Foundation (SNSF) for supporting this work. ML acknowledges the Centre National de la Recherche Scientifique (CNRS) and the Centre National des Etudes Spatiales (CNES) for support. MJ is supported by the United Kingdom Research and Innovation (UKRI) Future Leaders Fellowship ‘Using Cosmic Beasts to uncover the Nature of Dark Matter’ (grant number MR/X006069/1).

DATA AVAILABILITY

The measurements obtained in that work are available in the following [repository](#). In particular, we release a cluster member catalogue, with their light profile measurement, velocity dispersion and stellar masses. We also provide the empirical PSF and the masked F160W mosaic used in the light profile fitting procedure. For the BCG, we provide each MGE fit as well as the stellar kinematics and stellar masses. As the last two measurements have been obtained in elliptical bins from the MUSE datacube, we provide the mask of each bin.

REFERENCES

- Abell G. O., Corwin Harold G. J., Olowin R. P., 1989, *ApJS*, **70**, 1
- Amara A., Quanz S. P., 2012, *MNRAS*, **427**, 948
- Andrade K. E., Fuson J., Gad-Nasr S., Kong D., Minor Q., Roberts M. G., Kaplinghat M., 2022, *MNRAS*, **510**, 54
- Arnouts S., et al., 2013, *A&A*, **558**, A67
- Bacon R., et al., 2010, in McLean I. S., Ramsay S. K., Takami H., eds, *Society of Photo-Optical Instrumentation Engineers (SPIE) Conference Series Vol. 7735, Ground-based and Airborne Instrumentation for Astronomy III*. p. 773508 ([arXiv:2211.16795](#)), doi:10.1117/12.856027
- Bacon R., Piqueras L., Conseil S., Richard J., Shepherd M., 2016, *MPDAF: MUSE Python Data Analysis Framework*, *Astrophysics Source Code Library*, record ascl:1611.003
- Beauchesne B., 2025, A comprehensive separation of dark matter and baryonic mass components in galaxy clusters II: an overview of the mass distribution in Abell S1063
- Beauchesne B., et al., 2024, *MNRAS*, **527**, 3246
- Beauchesne B., et al., 2025, *MNRAS*, **536**, 2086
- Bergamini P., et al., 2019, *A&A*, **631**, A130
- Bertin E., Arnouts S., 1996, *A&AS*, **117**, 393
- Bertin E., Schefer M., Apostolakis N., Álvarez-Ayllón A., Dubath P., Kümmel M., 2020, in Pizzo R., Deul E. R., Mol J. D., de Plaa J., Verkouter H., eds, *Astronomical Society of the Pacific Conference Series Vol. 527, Astronomical Data Analysis Software and Systems XXIX*. p. 461
- Bonamigo M., et al., 2017, *ApJ*, **842**, 132
- Bonamigo M., et al., 2018, *ApJ*, **864**, 98
- Bradač M., Allen S. W., Treu T., Ebeling H., Massey R., Morris R. G., von der Linden A., Applegate D., 2008, *ApJ*, **687**, 959
- Bradbury J., et al., 2021, *JAX: Autograd and XLA*, *Astrophysics Source Code Library*, record ascl:2111.002
- Brownstein J. R., Moffat J. W., 2007, *MNRAS*, **382**, 29
- Bruzual G., Charlot S., 2003, *MNRAS*, **344**, 1000
- Buchner J., 2019, *PASP*, **131**, 108005
- Buchner J., 2021, *The Journal of Open Source Software*, **6**, 3001
- Buchner J., et al., 2014a, *A&A*, **564**, A125
- Buchner J., et al., 2014b, *A&A*, **564**, A125
- Calzetti D., Armus L., Bohlin R. C., Kinney A. L., Koornneef J., Storchi-Bergmann T., 2000, *ApJ*, **533**, 682
- Caminha G. B., et al., 2016, *A&A*, **587**, A80
- Cappellari M., 2002, *MNRAS*, **333**, 400
- Cappellari M., 2008, *MNRAS*, **390**, 71
- Cappellari M., 2017, *MNRAS*, **466**, 798
- Cappellari M., Copin Y., 2003, *MNRAS*, **342**, 345
- Carnall A. C., McLure R. J., Dunlop J. S., Davé R., 2018, *MNRAS*, **480**, 4379
- Carnall A. C., Leja J., Johnson B. D., McLure R. J., Dunlop J. S., Conroy C., 2019, *ApJ*, **873**, 44
- Carnall A. C., et al., 2023, *Nature*, **619**, 716
- Cerny C., Jauzac M., Lagattuta D., Niemiec A., Mahler G., Edge A., Massey R., 2025, *arXiv e-prints*, p. [arXiv:2506.21531](#)
- Chabrier G., 2003, *PASP*, **115**, 763
- Clowe D., Gonzalez A., Markevitch M., 2004, *ApJ*, **604**, 596
- Clowe D., Bradač M., Gonzalez A. H., Markevitch M., Randall S. W., Jones C., Zaritsky D., 2006, *ApJ*, **648**, L109
- Collett T. E., et al., 2018, *Science*, **360**, 1342
- Conroy C., 2013, *ARA&A*, **51**, 393
- Da Rocha C., Mendes de Oliveira C., 2005, *MNRAS*, **364**, 1069
- Dai D.-C., Matsuo R., Starkman G., 2008, *Phys. Rev. D*, **78**, 104004
- Diego J. M., Broadhurst T., Wong J., Silk J., Lim J., Zheng W., Lam D., Ford H., 2016, *MNRAS*, **459**, 3447
- Eckert D., Ettori S., Robertson A., Massey R., Pointecouteau E., Harvey D., McCarthy I. G., 2022, *A&A*, **666**, A41
- Ellien A., et al., 2021, *A&A*, **649**, A38
- Ettori S., Donnarumma A., Pointecouteau E., Reiprich T. H., Giodini S., Lovisari L., Schmidt R. W., 2013, *Space Sci. Rev.*, **177**, 119
- Evans I. N., et al., 2010, *ApJS*, **189**, 37
- Falcón-Barroso J., Sánchez-Blázquez P., Vazdekis A., Ricciardelli E., Cardiel N., Cenarro A. J., Gorgas J., Peletier R. F., 2011, *A&A*, **532**, A95
- Feroz F., Hobson M. P., Cameron E., Pettitt A. N., 2019, *The Open Journal of Astrophysics*, **2**, 10
- Giallongo E., et al., 2014, *ApJ*, **781**, 24
- Granata G., et al., 2022, *A&A*, **659**, A24
- Harvey D., Massey R., Kitching T., Taylor A., Tittley E., 2015, *Science*, **347**, 1462
- Herbel J., Kacprzak T., Amara A., Refregier A., Lucchi A., 2018, *J. Cosmology Astropart. Phys.*, **2018**, 054
- Horne K., 1986, *PASP*, **98**, 609
- Ilbert O., et al., 2015, *A&A*, **579**, A2
- Janowiecki S., Mihos J. C., Harding P., Feldmeier J. J., Rudick C., Morrison H., 2010, *ApJ*, **715**, 972
- Jiménez-Teja Y., Dupke R., 2016, *ApJ*, **820**, 49
- Johnson T. L., Sharon K., Bayliss M. B., Gladders M. D., Coe D., Ebeling H., 2014, *ApJ*, **797**, 48
- Kassiola A., Kovner I., 1993, *ApJ*, **417**, 450
- Kluge M., et al., 2020, *ApJS*, **247**, 43
- Kneib J.-P., Natarajan P., 2011, *A&ARv*, **19**, 47
- Koekemoer A. M., et al., 2011, *ApJS*, **197**, 36
- Kroupa P., 2001, *MNRAS*, **322**, 231
- Limousin M., Kneib J.-P., Natarajan P., 2005, *MNRAS*, **356**, 309
- Limousin M., Beauchesne B., Jullo E., 2022, *A&A*, **664**, A90
- Longobardi A., Arnaboldi M., Gerhard O., Pulsoni C., Söldner-Rembold I., 2018, *A&A*, **620**, A111
- Lotz J. M., et al., 2017, *ApJ*, **837**, 97
- Mamon G. A., 2022, *MAMPOSSt: Mass/orbit modeling of spherical systems*, *Astrophysics Source Code Library*, record ascl:2203.020
- Mamon G. A., Biviano A., Boué G., 2013, *Monthly Notices of the Royal Astronomical Society*, **429**, 3079–3098
- Meneghetti M., et al., 2020, *Science*, **369**, 1347
- Mercurio A., et al., 2021, *A&A*, **656**, A147
- Mlotshwa T., van Deventer H., Sergeevna Bosman A., 2023, *arXiv e-prints*, p. [arXiv:2302.07238](#)
- Monna A., et al., 2014, *MNRAS*, **438**, 1417
- Montes M., 2022, *Nature Astronomy*, **6**, 308
- Montes M., Trujillo I., 2014, *ApJ*, **794**, 137
- Montes M., Trujillo I., 2018, *MNRAS*, **474**, 917

Parameters	Cold	Hot
DETECT_MINAREA	5	5
DETECT_THRESH	5	1.8
ANALYSIS_THRESH	6	2
FILTER	Y	Y
FILTER_NAME	DEFAULT.CONV	DEFAULT.CONV
DEBLEND_NTHRESH	12	64
DEBLEND_MINCONT	0.001	0.0001
BACK_SIZE	32	32
BACK_FILTERSIZE	3	3
BACKPHOTO_TYPE	GLOBAL	GLOBAL

Table A1. SEXTTRACTOR parameters used in the cold and hot pass to create a catalogue for AS1063.

Morishita T., Abramson L. E., Treu T., Schmidt K. B., Vulcani B., Wang X., 2017, *ApJ*, **846**, 139
Natarajan P., et al., 2017, *MNRAS*, **468**, 1962
Natarajan P., Williams L. L. R., Bradač M., Grillo C., Ghosh A., Sharon K., Wagner J., 2024, *Space Sci. Rev.*, **220**, 19
Newman A. B., Treu T., Ellis R. S., Sand D. J., 2013, *ApJ*, **765**, 25
Pedregosa F., et al., 2011, *Journal of Machine Learning Research*, **12**, 2825
Postman M., et al., 2012, *ApJS*, **199**, 25
Richard J., et al., 2014, *MNRAS*, **444**, 268
Rix H.-W., et al., 2004, *ApJS*, **152**, 163
Robertson A., Massey R., Eke V., Schaye J., Theuns T., 2021, *MNRAS*, **501**, 4610
Sagunski L., Gad-Nasr S., Colquhoun B., Robertson A., Tulin S., 2021, *J. Cosmology Astropart. Phys.*, **2021**, 024
Serenio M., Lubini M., Jetzer P., 2010, *A&A*, **518**, A55
Sérsic J. L., 1963, *Boletín de la Asociación Argentina de Astronomía La Plata Argentina*, **6**, 41
Speagle J. S., Steinhardt C. L., Capak P. L., Silverman J. D., 2014, *ApJS*, **214**, 15
Spergel D. N., Steinhardt P. J., 2000, *Phys. Rev. Lett.*, **84**, 3760
Steinhardt C. L., et al., 2020, *ApJS*, **247**, 64
Tortorelli L., Mercurio A., 2023, *Frontiers in Astronomy and Space Sciences*, **10**, 51
Tortorelli L., et al., 2018, *MNRAS*, **477**, 648
Valdes F., Gupta R., Rose J. A., Singh H. P., Bell D. J., 2004, *ApJS*, **152**, 251
Virtanen P., et al., 2020, *Nature Methods*, **17**, 261
Willmer C. N. A., 2018, *ApJS*, **236**, 47
Xie Y., et al., 2024, *MNRAS*, **531**, 1179
Zitrin A., et al., 2015, *ApJ*, **801**, 44

APPENDIX A: SEXTTRACTOR PARAMETER

The SEXTTRACTOR parameters used in the cold and hot pass are listed in Table A1

APPENDIX B: LIGHT MODEL

As we automatically fit a large number of galaxies, we modify the analytical expression of the considered profiles so that there are no undefined points in our parameter bounds. This can obfuscate the meaning of the parameters, but it allows the code to avoid some crashes. The parameters are converted to the usual definitions after the fit.

The usual definitions of the Sérsic or dPIE profiles projected on

the plane of the sky are the following:

$$I_{\text{Srsic}} = I_0 \exp \left(-b_n \left[\left(\frac{R}{R_e} \right)^{1/n} - 1 \right] \right) \quad (\text{B1})$$

$$I_{\text{dPIE}} = \frac{\Sigma_0 r_{\text{cut}}}{r_{\text{cut}} - r_{\text{core}}} \left(\frac{1}{\sqrt{r_{\text{core}}^2 + R^2}} - \frac{1}{\sqrt{r_{\text{cut}}^2 + R^2}} \right) \quad (\text{B2})$$

where I_0 , R_e and n are the normalisation, half-light radius and the Sérsic index, respectively. They are the free parameters of the profile, and b_n can be computed as the solution of $\gamma(2n, b_n) = \Gamma(2n)/2$. For the dPIE profile, Σ_0 , r_{cut} and r_{core} are the normalisation, cut, and core radii, respectively.

To ensure a better parameter space and improve the computation speed for the Sérsic profile, we are not computing b_n as we replaced R_e with another parameter, h , that encompasses its values with R_e . We also replace n by $\beta = n^{-1}$ and I_0 with $I_{0,n} = I_0 \exp b_n$ such that we obtain:

$$I_{\text{Srsic}} = I_{0,n} \exp \left(-h R^\beta \right) \quad (\text{B3})$$

From this expression, we can then deduce the expression of h as $h = b_n R_e^{-1/n}$.

For the dPIE profile, we simplify the normalisation and switch r_{core} by a_{core} such that:

$$I_{\text{dPIE}} = \Sigma_0^* \left(\frac{1}{\sqrt{a_{\text{core}}^2 r_{\text{cut}}^2 + R^2}} - \frac{1}{\sqrt{r_{\text{cut}}^2 + R^2}} \right) \quad (\text{B4})$$

With the following expression for a_{core} and Σ_0^* :

$$a_{\text{core}} = r_{\text{core}} / r_{\text{cut}} \quad (\text{B5})$$

$$\Sigma_0^* = \frac{\Sigma_0 r_{\text{cut}}}{r_{\text{cut}} - r_{\text{core}}} \quad (\text{B6})$$

$$(\text{B7})$$

Thanks to our redefinition of the dPIE parameter, we can ensure that $r_{\text{cut}} > r_{\text{core}}$ by letting a_{core} in $]0, 1[$.

APPENDIX C: FIT ON REGIONS STAMP: INITIAL PARAMETER ESTIMATION

In section 4.1.2, we detail our procedure to fit multiple objects light distributions in a postage stamp image. The optimisation procedure is based on a non-linear least-square algorithm, which requires a guess for light model parameters as a starting point. For the coordinates centre, position angle and ellipticity, we are using SEXTTRACTOR measurements of XWIN_IMAGE, YWIN_IMAGE, THETAWIN_IMAGE, AWIN_IMAGE and BWIN_IMAGE. For the Sérsic profile, we start with an index $n = 2.5$, FLUX_RADIUS measurements for R_e , and we estimate I_0 based on the MAG_BEST values. These parameters are then converted to our effective parameters defined in Sect. B. To adopt similar starting points for dPIE, we fit dPIE profiles in 1D on a Sérsic profile with the previous parameter set. We use the fit output as a starting point for the least-square fit.

Regarding the parameter bound, we choose to use large bounds to avoid hitting them as we ensure some safety against invalid parameter sets with our re-definition of the light profile. Except for the coordinate centre which we impose around the SEXTTRACTOR estimation.

The bounds are defined as follows:

$$\text{axis ratio} : \mathcal{U}(1, 20) \quad (\text{C1})$$

$$x_c : \mathcal{U}(x_{c,\text{init}} - 1, x_{c,\text{init}} + 1) \quad (\text{C2})$$

$$y_c : \mathcal{U}(y_{c,\text{init}} - 1, y_{c,\text{init}} + 1) \quad (\text{C3})$$

$$\theta : \mathcal{U}(-\pi/2, \pi) \quad (\text{C4})$$

$$h : \mathcal{U}(0, 100h_{\text{init}}) \quad (\text{C5})$$

$$\beta : \mathcal{U}(0.1, 5) \quad (\text{C6})$$

$$I_{0,n} : \mathcal{U}(0, I_{0,n}^{\text{init}}) \quad (\text{C7})$$

$$a_{\text{core}} : \mathcal{U}(0, 1) \quad (\text{C8})$$

$$r_{\text{cut}} : \mathcal{U}(0, 100r_{\text{cut,init}}) \quad (\text{C9})$$

$$\Sigma_0^* : \mathcal{U}(0, 100\Sigma_{0,\text{init}}^*) \quad (\text{C10})$$

We note that in some cases, these bounds were too large and caused issues to converge for faint objects or in particularly crowded spaces. The main parameters in question are the axis ratio and h or r_{cut} , which tend to converge to overestimated values. The light distribution of these objects was set to zero when a light model was subtracted during the Bayesian inference.

APPENDIX D: BAYESIAN INFERENCE: PRIOR

Following the non-linear least-square fit, we perform a Bayesian inference as detailed in Sect. 4.1.3. For the prior, we use uniform priors for all parameters. We re-use the bounds defined in the previous section for most parameters except Σ_0^* , r_{cut} , h and $I_{0,n}$. For these last parameters, we compute their statistical errors from the least-square fit, and we redefine their bound such that it is centred among the best-fitting solutions from the least-square with a width on each side equal to 5 times the statistical error. We ensure that these bounds are included in the least-square bounds to avoid enlarging them when the statistical errors have large values.

As stated in Sect. C, some of the bounds are too large, which prevents convergence from reaching a good solution. Hence, for some objects, we manually change the bounds associated with the axis ratio and h or r_{cut} . As all fits are independent, it does not have an effect on neighbouring objects.

This paper has been typeset from a \LaTeX file prepared by the author.